Published OnlineFirst December 1, 2020; DOI: 10.1158/0008-5472.CAN-20-0373

Preclinical Applications of Multi-Platform Imaging in Animal Models of Cancer

Natalie J. Serkova[1,2], Kristine Glunde[3], Chad R. Haney[4], Mohammed Farhoud[5], Alexandra De Lille[6], Elizabeth F. Redente[7], Dmitri Simberg[8], David C. Westerly[2,9], Lynn Griffin[10], and Ralph P. Mason[11]

ABSTRACT

In animal models of cancer, oncologic imaging has evolved from a simple assessment of tumor location and size to sophisticated multimodality exploration of molecular, physiologic, genetic, immunologic, and biochemical events at microscopic to macroscopic levels, performed noninvasively and sometimes in real time. Here, we briefly review animal imaging technology and molecular imaging probes together with selected applications from recent literature. Fast and sensitive optical imaging is primarily used to track luciferase-expressing tumor cells, image molecular targets with fluorescence probes, and to report on metabolic and physiologic phenotypes using smart switchable luminescent probes. MicroPET/single-photon emission CT have proven to be two of the most translational modalities for molecular and metabolic imaging of cancers: immuno-PET is a promising and rapidly evolving area of imaging research. Sophisticated MRI techniques provide high-resolution images of small metastases, tumor inflammation, perfusion, oxygenation, and acidity. Disseminated tumors to the bone and lung are easily detected by microCT, while ultrasound provides real-time visualization of tumor vasculature and perfusion. Recently available photoacoustic imaging provides real-time evaluation of vascular patency, oxygenation, and nanoparticle distributions. New hybrid instruments, such as PET-MRI, promise more convenient combination of the capabilities of each modality, enabling enhanced research efficacy and throughput.

Introduction

Recent technological developments in scanner design and advances in image reconstruction have secured the rapid application of noninvasive imaging for detection, characterization, and monitoring of cancer etiology in a variety of animal models (1–3). Obvious advantages arise from the ability to study structure, metabolism, and function of cancer cells and cancer supporting microenvironment longitudinally, without the need for necropsy. Indeed, imaging is noninvasive and repetitive studies are performed in the same animals, with each animal serving as its own control. Importantly, most imaging platforms can efficiently survey whole animals, opening new horizons for studying metastatic disease. Furthermore, many imaging technologies are intrinsically translational by applying identical imaging protocols, imaging tracers, and image analysis to various species, thereby providing a bridge from laboratory animals to companion animals and ultimately to humans with the goal of easing the burden of human cancer (4–6). There are various imaging platforms, also referred to as imaging modalities, each based on a specific physical principle (**Table 1**), allowing unique information/data to be generated. The primary reason for applying a multi-platform imaging approach to cancer research is to obtain comprehensive information from a cancer-bearing animal (**Table 2**). The *in vivo* cancer imaging modalities are highly complementary, providing a variety of quantitative biomarkers for cancer cell tracking, and assessing tumor dimensions, pathophysiology, metabolism, and molecular composition (**Table 2**; **Fig. 1**), but each has specific advantages and weaknesses (6–8). In this review, we highlight the state-of-the-art applications of preclinical multimodal multiscale imaging and focus on the specific applicability to cancer research.

MRI and Spectroscopy

Magnetic resonance (MR) physics is complicated, but offers extraordinary opportunities to manipulate tissue water signals based on relaxation mechanisms, chemical exchange, flow, and diffusion to reveal diverse anatomic, physiologic, and cellular properties of cancer at high external magnetic fields. The most sensitive nucleus is the proton, notably in H_2O. Anatomic MRI: among all imaging modalities, MRI possesses the best soft-tissue contrast, which may still be enhanced further using exogenous paramagnetic contrast agents. Excellent spatial resolution can reveal ultra-small cancer lesions (as small as 0.2-mm diameter with 9.4 T MRI), particularly in well-structured tissues, such as the brain. MRI is the "gold-standard" for orthotopic brain tumors and brain metastases (**Fig. 1A**, **1**; refs. 9–13), and is also widely applied for the detection of other soft-tissue lesions, including liver (**Fig. 1A**, **2**) and lung metastases (**Fig. 1A**, **3**). Physiologic MRI: beyond high-resolution anatomic MRI, tumor cellular density and edema are easily quantified using diffusion-weighted MRI, which is sensitive to restricted or enhanced diffusion of water molecules, respectively (**Fig. 1B**, **7**; refs. 2, 14, 15). Several recent publications reported increased apparent diffusion coefficients (ADC)

[1]Department of Radiology, University of Colorado Anschutz Medical Campus, Aurora, Colorado. [2]Animal Imaging Shared Resource, University of Colorado Cancer Center, Aurora, Colorado. [3]Division of Cancer Imaging Research, The Russell H. Morgan Department of Radiology, and the Sydney Kimmel Comprehensive Cancer Center, Johns Hopkins Medical Institutions, Baltimore, Maryland. [4]Center for Advanced Molecular Imaging, Northwestern University, Evanston, Illinois. [5]Emit Imaging, Boston, Massachusetts. [6]SonoVol, Durham, North Carolina. [7]Department of Pediatrics, National Jewish Health, Denver, Colorado. [8]Department of Pharmaceutical Sciences, University of Colorado Anschutz Medical Campus, Aurora, Colorado. [9]Department of Radiation Oncology, University of Colorado Anschutz Medical Campus, Aurora, Colorado. [10]Department of Radiology, Veterinary Teaching Hospital, Colorado State University, Fort Collins, Colorado. [11]Department of Radiology, University of Texas Southwestern, Dallas, Texas.

Corresponding Author: Natalie J. Serkova, University of Colorado Anschutz Medical Campus and University of Colorado Cancer Center, 12631 E. 17th Avenue, Suite L15-2004, P. O. Box 6511, Aurora, CO 80045. Phone: 303-724-1086; Fax: 303-724-1761; E-mail: natalie.serkova@CUAnschutz.edu

Cancer Res 2021;81:1189–200

doi: 10.1158/0008-5472.CAN-20-0373

Published OnlineFirst December 1, 2020; DOI: 10.1158/0008-5472.CAN-20-0373

Table 1. Physical principles of the main preclinical imaging modalities and their basic characteristics.

Modality	Physical principles	Whole-body/target organ	Resolution scale
MRI/MRS	External magnetic field; nuclear spin; radio wave pulses (for magnetization of hydrogens in tissue water/metabolites)	4–6 cm FOV: brain, heart, liver, pancreas, muscle	35–150 μm
microCT	3-Dimensional X-ray beam absorption and scattering	Whole body/lung, bone	10–50 μm
US	Reflection of high-frequency sound waves	2–4 cm FOV: heart, pelvic, liver, pancreas, OBGYN	60–120 μm
Photoacoustic (PAI, MSOT)	Spectrally selective near-infrared light excitation of chromophores, inducing sound waves, providing tomographic images; notably oxy-deoxyhemoglobin, exogenous 800CW-tagged agents and gold nanoparticles	Tomographic slices of whole mouse or larger animal to 4 cm depth; breast, thyroid	150 μm; 100 milliseconds
Optical: BLI and FLI	Light emitting chemical reaction, often enzyme facilitated, e.g., luciferin/luciferase; photo-stimulated fluorescence chromophores	Whole body	mm, depth dependent
PET/SPECT	Decay of short-lived radioactive beta+ and photon emitters	Whole body	1.0–1.8 mm

Abbreviations: FOV, field of view; OBGYN, obstetrics and gynecology.

associated with treatment-induced necrosis (16–19). Tissue oxygenation may be examined using oxygen-sensitive MRI. Notably, apparent transverse relaxation rate (R_2^*) is sensitive to the concentration of deoxyhemoglobin, as exploited in blood oxygen level–dependent (BOLD) contrast and forming the basis of functional MRI to assess neurologic activation (20). Meanwhile, so-called tissue oxygen level–dependent (TOLD) MRI exploits the sensitivity of the spin-lattice relaxation rate, R_1, to the paramagnetic oxygen molecule (O_2) itself (**Fig. 1B**, **8**; refs. 21–27). Noting the importance of hypoxia in cancer development, aggressiveness, and response to therapy, an oxygen gas breathing challenge has been shown to provide a simple effective theranostic: well-oxygenated tissues show response to an oxygen gas breathing challenge, whereas hypoxic tissue does not (28). This approach has been demonstrated to provide a prognostic imaging biomarker in rats with respect to stereotactic ablative radiotherapy (24, 28) and is feasible in man (21, 29). Vascular MRI: the use of exogenous MR contrast agents, namely gadolinium chelates as T_1- and iron oxide nanoparticles as T_2-contrast, enables imaging of tumor angiogenesis and changes in tumor vascularity. Intravenous injection of gadolinium contrast agent allows direct visualization of tumor vasculature by MR angiography (MRA, **Fig. 1C**, **11**; ref. 30) or the generation of tumor perfusion/permeability K^{trans} maps using dynamic contrast-enhanced (DCE)-MRI (**Fig. 1C**, **12**; refs. 31–33). The use of T_2-contrast blood pool agents (based on ferumoxytol and other iron oxide nanoparticles) allows susceptibility-contrast imaging to assess tumor blood volume (32, 34). Cellular and receptor MRI: the same iron oxide nanoparticles can be used for cell tracking. Breast cancer cells prelabeled with ferumoxytol *in vitro*, could be detected in the brain by T_2-MRI following intravenous injection (**Fig. 1E**, **21**; ref. 35). Meanwhile, injection of ferumoxytol itself leads to extensive uptake by macrophages, which has been observed as reduced T_2 signal, revealing M1 (antitumor) or M2 (pretumor) activity (**Fig. 1E**, **22**; refs. 36–38). Some reports have explored the possibilities of using iron oxide- or gadolinium-based contrast for detecting cell receptors, including HER2 or C2 imaging in mouse models of breast cancer and precancerous renal inflammation (39–41). In mouse prostate cancer models, prostate specific membrane antigen (PSMA) receptors have been successfully imaged using targeted iron oxide nanoparticles by T_2-MRI or a diamagnetic dextran-based chemical exchange saturation transfer (CEST) MRI agent (see below; refs. 42–44). Receptor imaging with MRI poses unique challenges for signal amplification to deposit sufficient MRI contrast per receptor molecule for its detection.

Other nuclei and metabolic MR spectroscopy

Beyond proton MRI of tissue water, spectroscopic imaging can detect several endogenous metabolites that occur at sufficiently high

Table 2. The ultimate guide for choosing a specific imaging platform in a cancer research study design.

Tumor etiology	Appropriate imaging modality to assess tumor characteristics	Quantitative imaging biomarkers
Dimensions	CT, T_1/T_2-MRI, US	Tumor volume, mm^3 Tumor diameter, mm
Cellularity	Diffusion-weighted MRI	ADC
Proliferation	^{18}FLT-PET	Standard uptake values (SUV)
Metastases	CT, MRI → BLI, PET	Number of lesions → qualitative
Vascularity/oxygenation/hypoxia	MRA, DCE, CE-CT, PAI sO_2-MSOT	Exchange rate constants: K^{trans} and V_e
	Oxygen-enhanced MRI (BOLD/TOLD), ^{18}F-MISO, ^{18}F-FAZA PET	ΔR_2^* maps, ΔR_1, AUC, tBV HbO_2; SO_2^{MSOT}; SUV
Metabolism/tumor pH	PET, FLI	SUVs, SIs
	^{1}H-MRSI, hyperpolarized ^{13}C-MRSI, ^{31}P-MRS, ^{19}F-MRS	Metabolite concentrations, metabolite ratios, metabolite maps
	pH: ^{31}P-MRS, CEST-MRI	Intra-extracellular pH values and pH maps
Inflammation	ImmunoPET, iron oxide NP T_2-MRI, PFC ^{19}F-MRI, EPR	SUVs, ΔT_2 relaxation times
Redox imaging		SIs
Cellular tracking	BLI, ^{19}F-MRI, iron oxide T_2-MRI, PET	SIs, SUVs
Molecular targets	SPECT, PET, BLI, FLI	SUVs, SIs → qualitative

Abbreviations: MSOT, multispectral optoacoustic tomography; NP, nanoparticle; PFC, perfluorocarbon nanoparticle; tBV, tumor blood volume.

Published OnlineFirst December 1, 2020; DOI: 10.1158/0008-5472.CAN-20-0373

concentrations, such as lactate, glutamine, glutamate, creatine, N-acetyl aspartate, γ-aminobutyric acid, citrate, choline, and, most recently, 2-hydroxyglutarate (2HG; ref. 45). The oncometabolite 2HG accumulates in low-grade glioma, secondary glioblastoma, and acute myeloid leukemia, owing to mutations in the metabolic enzymes isocitrate dehydrogenase (IDH) 1 or 2. Mutant IDH1/2 aberrantly produces 2HG (instead of ketoglutarate), which is detectable by ^{1}H-MRS or ^{13}C-magnetic resonance spectroscopic imaging (MRSI) following hyperpolarized [1-^{13}C]-glutamine administration (**Fig. 1D**, **17**; ref. 46). For ^{13}C-MRSI, the most developed hyperpolarized probe today is [1-^{13}C]-pyruvate, which enables the detection of activated lactate dehydrogenase in tumors (47). Isotopically labeled substrates and metabolites are clearly seen against naturally low abundance endogenous signals (e.g., 100% enriched isotopomers vs. 1.1% naturally abundant ^{13}C). Furthermore, hyperpolarization of ^{13}C substrates can be achieved by various techniques, including dynamic hyperpolarization (48) or parahydrogen-induced polarization (49) and leads to a significant boost in the naturally low ^{13}C MR spectroscopy (MRS) signal. However, magnetization decays rapidly within minutes, necessitating fast ^{13}C MRI techniques. It has been shown that hyperpolarized ^{13}C-pyruvate/lactate MRS(I) is superior to 2[^{18}F]fluoro-2-deoxy-D-glucose ^{18}FDG-PET (another metabolic imaging technique, see below) in detecting treatment response to novel targeted therapies and radiation (50, 51). Another approach to amplify MRS signals uses CEST MRI, which detects the exchange of protons from hydroxyl, amine, and amide groups to tissue water through the transfer of signal loss, with repeated proton exchange enhancing the effective signal in endogenous (52) and exogenous compounds (**Fig. 1D**, **18**; ref. 53). Amide proton transfer contrast, which is the CEST signal from endogenous cellular proteins and peptides, differentiates viable glioma from radiation necrosis (54). The use of D-glucose administration as a contrast agent for noninvasive CEST detection of tumors has been termed glucoCEST, and offers cancer detection with glucose as a biodegradable, nontoxic contrast agent (55). CEST measurements of regional pH, on the basis of the clinically approved X-ray contrast agent, iopamidol, have been applied in kidney and lung cancer models (56, 57). Another important nucleus for cancer characterization by MRS is ^{31}P for detection of phospholipid precursors, high energy phosphates, and inorganic phosphate, which exhibits a pH-sensitive chemical shift in the physiologic range (58), although it can be difficult to discriminate intra- versus extracellular components. Meanwhile, ^{19}F-MR agents can offer superior chemical shift response (59). ^{19}F-MRI with perfluorocarbon agents has been used as an alternative to iron oxide T_2-MRI (see above and **Fig. 1E**, **22**) to detect tumor-associated macrophages with the benefit of no endogenous background signal (60). Perfluorocarbons exhibit very high gas solubility and can serve as molecular amplifiers, as exploited to assess tumor pO_2 providing evidence for hypoxia, heterogeneity, and differential regional response to interventions (28, 59, 61).

X-ray CT

X-ray CT (microCT) is a high-resolution 3-dimensional (3D) imaging technique; the physical principle of CT is based on scattering and absorption of X-rays by tissues based on their electron density. There are essentially three levels of attenuation yielding color-coded contrast in CT: air (black), soft-tissue (gray shades), and bones (white). Anatomic microCT: compared with MRI, CT is inferior in distinguishing soft tissues/organs, but the major strength of microCT lies in supreme high-resolution (<50 μm) fast imaging of lungs and bones revealing cancer lesions. Because bones are the most common metastatic site for major cancers (including breast and prostate), several studies reported the use of high-resolution (10 μm) microCT for detecting engrafted breast cancer cells in the bone (**Fig. 1A**, **4**; ref. 62). Inhibition of the development of osteolytic bone lesions by zoledronic acid has been reported in MDA-MB-231 breast xenograft mice, also identifying IL1 as one of the key players for metastatic development (63–65). Because of the inherent contrast between air and tissue structures and the resulting attenuation of the X-rays passing through tissue, microCT is particularly well suited for providing high-quality anatomic information in the lung. With the development of precancerous lung conditions, including inflammation (66), fibrosis (67), and emphysema (68), and their progression to lung tumors (69–71), tissue structure becomes dense and can be easily differentiated from both normal lung and airspace. The use of 3D analysis to quantify tumor number, size, and progression is advantageous over traditional histology (69) or macrodissection of the lung to isolate tumors (70). Vascular microCT: gated respiratory-holding techniques, fast acquisition times, and the introduction of novel metal nanoparticles, such as exitron, allow lung microvasculature to be easily visualized, simultaneously with lung tumor detection (**Fig. 1C**, **13**; refs. 72, 73). The low radiation dose of modern instruments makes longitudinal microCT possible without long-term harm to animals (74). Recently, contrast-enhanced microCT has been applied to visualize and map tumor vasculature in brain tumor and neuroblastoma mouse models (75–77).

Ultrasound

Ultrasound (US) uses high-frequency sound waves and captures the US energy reflected from interfaces in the body ("echoes") that separate tissue with different acoustic impedances, where the acoustic impedance is the product of physical density and velocity of sound in the tissue. Typically, a cyst appears sonolucent, because it gives few, if any, echoes (being mostly water), while liver and spleen have solid homogenous echo texture due to medium-level echoes from the fibrous interstitial tissues. High-intensity echoes (increased echogenicity) are caused by calcification, fat, and air interface; however, they do not propagate through bone. Among real-time modalities, US features the highest frame rate up to 20,000 fps, enabling US-guided animal procedures, such as orthotopic cell tumor injections and left ventricular infusion of cancer cells, to generate models of metastasis while avoiding lung engraftment (78, 79). Anatomic US: pancreatic cancer is one of the most challenging mouse models for preclinical imaging. US provides fast, precise quantification of pancreatic tumor burden longitudinally and without contrast administration (**Fig. 1A**, **6**; refs. 80, 81). Vascular US: US is also an excellent technique to assess tumor vasculature, for example, Doppler US measures the speed and direction of flowing blood and has revealed vascular response to antiangiogenic and Notch therapies in an orthotopic renal cell carcinoma mouse model (82), as well as in irradiated rat fibrosarcoma tumors (83). Considerable attention has been given to the development of US-specific nanoparticles and microbubbles, which may be used both for vascular imaging and as theranostic drug carriers. The latest include VEGFR2-targeted microbubbles (84), oxygen microbubbles (85, 86), and US-destructible microbubbles for better delivery of paclitaxel-loaded nanoparticles in pancreatic cancer models (87). Acoustic angiography (AA) is another contrast-enhanced US technique, which uses the super-harmonic signals from microbubbles to produce high-resolution maps of vasculature with exceptional contrast because tissue yields no signal. Furthermore, AA can provide quantitative measurements of vascular

Published OnlineFirst December 1, 2020; DOI: 10.1158/0008-5472.CAN-20-0373

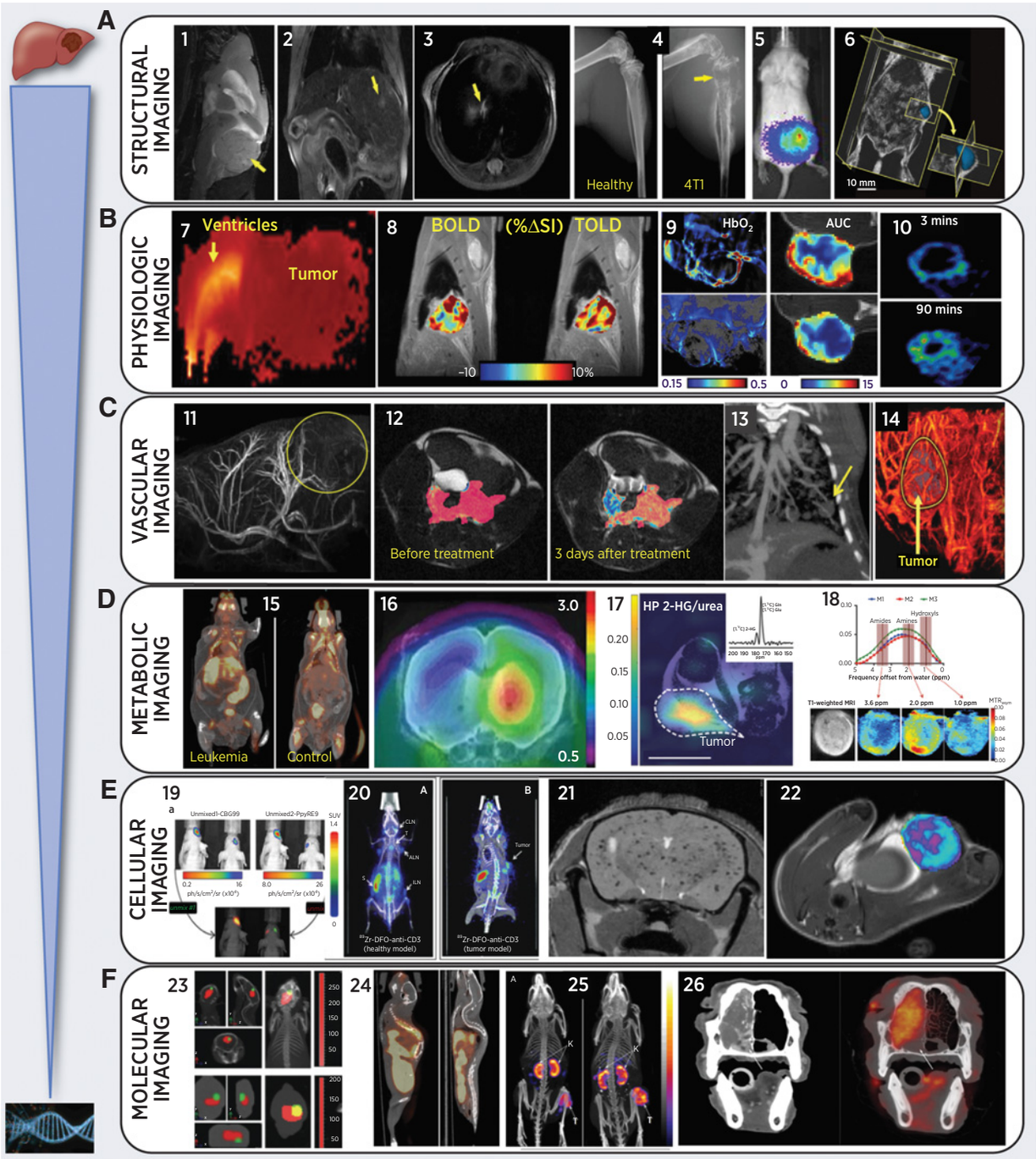

Figure 1.

Representative multimodality images of animal cancer models (from left to right): **A,** Anatomic cancer detection in mouse models: (**1**) T_2-weighted MRI of pediatric cerebellar brain tumor (medulloblastoma) patient-derived xenograft; (**2**) gadolinium-enhanced T_1-MRI of an orthotopic liver HCC; (**3**) proton density MRI of a lung metastasis from breast cancer; (**4**) microCT of bone metastasis from engrafted breast cancer cells, adapted from ref. 62; (**5**) BLI of multi-organ breast cancer metastases, adapted from ref. 62; and (**6**) 3D US of a murine mammary gland tumor. **B,** Physiology-based images in rodent cancer models: (**7**) high ADC (brain edema and ventricle hydrocephalus) and low ADC (highly proliferative medulloblastoma mouse patient-derived xenograft) from diffusion-weighted MRI; (**8**) BOLD and TOLD MRI in response to oxygen gas breathing challenge in orthotopic human A549 lung tumor xenograft in nude rat, adapted from ref. 23; (**9**) PAI of subcutaneous A549 human lung tumor growing in leg of nude rat showing endogenous HbO_2 concentration before (top) and 48 hours after (bottom) administration of VDA, based on multiple wavelengths (MSOT), while breathing O_2 (left) and corresponding DCE-MRI showing AUC reflecting reduced perfusion after VDA (right); and (**10**) ^{18}F-MISO (hypoxia tracer) PET in a syngeneic Dunning R3327-AT1 rat prostate tumor, adapted from ref. 143. **C,** Imaging tumor vasculature *in vivo*: (**11**) high-resolution MRA after gadolinium injection in an orthotopic rat isograft C6 glioma model; (**12**) DCE-MRI during gadolinium injection in mouse TRAMP model for prostate cancer, adapted from ref. 33; (**13**) contrast-enhanced microCT of lung vasculature and small lung tumor using liposomal-iodinated contrast agent, adapted from ref. 72; and (**14**) US enhanced with microbubbles reveals high perfusion in the rim of a flank pancreatic cancer xenograft in a mouse. (*Continued on the following page.*)

density, blood perfusion, and vessel morphology, helpful to evaluate response to antiangiogenic therapy in cancer (82). Quantitative US (88) is obtained from B-mode images and raw radiofrequency data and has been used to examine treatment response. Attenuation coefficients and backscatter coefficients can be derived (89). On the other hand, US elastography can visualize and quantify tissue stiffness noninvasively (90). These data can be used as a potential biomarker to assess changes in the tumor microenvironment, particularly changes affecting the extracellular matrix, which may affect treatment efficacy (91, 92).

Photoacoustic Imaging

Photoacoustic imaging (PAI) represents the newest addition to the commercial armamentarium for preclinical imaging studies and progressively experimental investigations in man (93, 94). PAI exploits spectrally selective pulsed laser excitation of chromophores generating local thermoelastic tissue expansion, which is detected on the basis of the resultant US acoustic waves, analogous to lightning generating thunder. Application of multiple wavelengths allows spectral discrimination, which has been applied to endogenous molecules, such as oxy- and deoxyhemoglobin (HbO_2 and Hb) and melanin, and exogenous agents, such as organic dyes, gold nanoparticles, and genetically encoded proteins (95, 96). Indeed, spectral unmixing allows multiple materials to be detected simultaneously. The technology is particularly rapid, typically achieving single-slice images in <100 milliseconds, but usually images are acquired at multiple wavelengths, and signals may be averaged so that a typical acquisition time is 1–2 seconds. Gating may become relevant for assessing rapid changes in tissues subject to motion (97). Selection of an appropriate nonnegative data reconstruction model is vital and choice of filters can enhance signal to noise (98, 99).

Various commercial instruments are optimized for *in vivo* microscopic, mesoscopic, whole-mouse tomographic, and human applications, and may incorporate additional US excitation to enhance anatomic discrimination with typical spatial resolution approaching 100 μm at depths up to 5 cm.

The most effective application is assessment of tumor vasculature based on the ability to identify and quantify relative Hb and HbO_2 (**Fig. 1B**, **9**) with effective studies of antiangiogenic therapy (100), acute vascular disruption induced by combretastatin (101, 102), and potentially prognostic observations following tumor irradiation (103). It appears that response to an oxygen breathing challenge characterized as ΔsO_2 is more closely related to perfusion and hypoxia than baseline static parameters (102), for example, low CAIX expression correlated with higher ΔsO_2^{MSOT}. Blood volume and perfusion may be effectively examined using contrast agents, such as indocyanine green (102, 104), or the liposomal formulation, Genhance (105). Small-molecule dyes may be incorporated in targeted liposomal formulations or used to directly label antibodies for detection of tumors or revealing receptor expression (106). Gold nanoparticles (which could also be used in microCT) exhibit exceptionally high photoacoustic activity based on surface plasmon resonance and may be tuned to wavelengths in the range 600–1,000 nm based on size and shape (96, 107). Additional innovations include "smart" activatable probes, for example, sensitive to β-galactosidase activation (108) and genetically encoded proteins, such as BphP1 (109). PAI essentially bridges two modalities to exploit spectrally selective optical excitation and robust spatial detection using US. It is very much an emerging technology.

Optical Imaging: Bioluminescence and Fluorescence

Two decades after its invention, *in vivo* optical imaging is now a well-established standard method to noninvasively monitor biological activity in mouse (and rat) research models. Optical imaging includes four molecular imaging modalities: bioluminescence imaging (BLI), fluorescence imaging (FLI), chemiluminescence, and Cherenkov imaging. The relatively low threshold of implementation, as well as the high sensitivity of *in vivo* BLI, make this whole-body, noninvasive imaging technique a go-to method in preclinical research (**Fig. 1A**, **5** and **E**, **19**; refs. 62, 110). Beyond tracking tumor growth and regression via constitutive firefly luciferase expression for drug efficacy determination, the toolbox for this molecular imaging technique has vastly expanded. Bioluminescence enzymes can be used to genetically tag cells, viruses, bacteria, gene therapy, and, now also, antibodies and their fragments (111). These enzymes, such as firefly, *Renilla*, *Gaussia*, and *NanoLuc* luciferases, can be constitutively or inducibly expressed, and as such used for ratiometric imaging, gene expression studies, or dual labeling purposes (e.g., tracking T cells infiltrating tumor; **Fig. 1E**, **19**; refs. 12, 112–114). Split luciferases to evaluate protein–protein interaction, as well as split luciferin substrates to monitor apoptosis have been designed and are utilized to evaluate mechanism of action (115). Potential drawbacks of BLI are the need for cell transfection and delivery of reactive substrate. Luciferin effectively crosses barriers, such as blood–brain and placenta, and its very delivery to tissue has been used to assess selective vascular destruction in tumors (101, 116). Bioluminescence resonance energy transfer constructs, such as Antares, which red shifts the shorter wavelength *NanoLuc* luciferase for better *in vivo* sensitivity, are also available (117). Chemiluminescence compounds, substrates, and sensors are

(*Continued.*) **D,** Imaging tumor metabolism noninvasively: (**15**) abnormal ^{18}F-FDG uptake in spleen, liver, and lymph nodes in transgenic leukemic (left) versus control mouse, adapted from ref. 129; (**16**) increased gliobastoma multiforme uptake of ^{18}F-ethyltyrosine without (left) and with bevacizumab treatment in an orthotopic U87 glioma mouse model, adapted from ref. 138; (**17**) representative heatmap of spectral data from a mouse with a mutant IDH1 tumor xenograft following injection of hyperpolarized [1-^{13}C]-glutamine showing accumulation of 2HG in the tumor region only, which was referenced and normalized to a 5 mmol/L [1-^{13}C] urea phantom. Dotted lines highlight the tumor, and the white line at the bottom represents 10 mm for scaling, adapted from ref. 46. (**18**) *In vivo* CEST-MRI of MDA-MB-231 breast tumor xenografts showing representative CEST MRI maps (top row, **A**), T_1-weighted RARE MRI (bottom left, **B**), and MTR_{asym} for three individual mice with orthotopic human MDA-MB-231 breast tumor xenografts, which were labeled M1 for mouse 1, M2 for mouse 2, and M3 for mouse 3. CEST shifts of amide, amine, and hydroxyl resonances are highlighted in **C**, adapted from ref. 52. **E,** Cellular tracking using noninvasive imaging in mouse cancer models: (**19**) dual reporter BLI using spectral unmixing algorithm. CBG99 cells were transplanted into the right striatum and PpyRE9 cells into the left striatum of the nude mouse on the right. A spectral unmixing algorithm was applied to select green light from CBG99 and red light from PpyRE9, adapted from ref. 191; (**20**) immuno-PET to image T lymphocytes using ^{89}Zr-anti-CD3 in normal (**A**) and BBN975 bladder cancer tumor-bearing (**B**) mice, adapted from ref. 147; (**21**) T_2-weighted brain MRI of ferumoxytol-labeled breast cancer cells after intracardiac injection, adapted from ref. 35; and (**22**) T_2-weighted maps for macrophage imaging after ferumoxytol injection in inflamed mammary gland tumor mouse model, adapted from ref. 37. CLN, cervical lymph node; ALN, axillary lymph node; ILN, inguinal lymph node; T, thymus; S, spleen. **F,** Molecular imaging of tumor-specific molecules: (**23**) tracking fluorescent micelles (red signal) to bioluminescent brain tumors (green) in anatomic context (124); (**24**) whole-body ^{18}F-estradiol (FES) PET/CT of ER in ER-positive and -negative bone metastases in mouse models of breast cancer; (**25**) whole-body SPECT/CT with ^{111}In-MSH peptide (melanocyte stimulating hormone) to image melanocortin-1 receptor in mouse B16/F1 melanoma model, adapted from ref. 154; and (**26**) CT and ^{18}FDG-PET of nasal adenocarcinoma in a canine patient with cancer (a 10-year-old standard poodle), adapted from ref. 187.

Published OnlineFirst December 1, 2020; DOI: 10.1158/0008-5472.CAN-20-0373

luminophores that emit red shifted light upon chemiexcitation and have been reported for detection of H_2O_2, H_2S, formaldehyde, β-galactosidase, and nitroreductase activity (118–121). Dr. Cherenkov received the Nobel Prize in 1958 for his discovery of the bluish hue of light emitted by decaying radioisotopes. This same light emission can be detected by screening mice injected with diagnostic radioisotopes, such as ^{18}FDG, in an *in vivo* optical imaging system, adopting the epithet of a poor man's PET scanner (122), and may also be relevant for radiation dosimetry (123). FLI, on the other hand, features both genetically encoded fluorescent proteins (FP) and fluorescent dyes. The powerful combination of BLI and FLI is exemplified by Zeng and colleagues (**Fig. 1F**, **23**; ref. 124), illustrating the tracking of fluorescent micelles to bioluminescent brain tumors. In comparison with BLI, however, the contrast to noise is less with fluorescence due to nonspecific autofluorescent noise originating from innate proteins in tissue. This issue is being combatted with the discovery of red-shifted FPs for better *in vivo* sensitivity, an initiative led by Nobel laureate Dr. Roger Tsien (125). A second window of opportunity for *in vivo* FLI is currently being explored in the short wavelength infrared using ultra-bright near-infrared-IIb rare-earth nanoparticles. Here, tissue absorption and light scattering are significantly reduced (126), rendering higher resolution, higher depth penetration images. Crafty alternatives have also been invented in which fluorescent sensors are quenched until activated by an enzymatic reaction (e.g., cathepsin, matrix metalloprotease, neutrophil elastase, etc.) or in which fluorophores shift wavelength upon binding their target (127). A great advantage of fluorophores is that they are also readily detectable *ex vivo* for histopathologic evaluation. This is highly translational, and intrasurgical fluorescence imaging is actively being explored to both highlight tumor burden, and also improve tumor margin of resection (128). Preclinical optical cancer imaging begs for anatomic context, prompting coregistration with anatomic imaging modalities, such as X-ray, microCT, MRI, or, the recently developed, robotic US, which features inexpensive, exogenous contrast-free 3D soft-tissue resolution (78).

PET and Single-Photon Emission CT

Nuclear medicine images are produced by giving the animal short-lived radioactive isotopes and detecting their decay using a gamma camera (single-photon emission CT, SPECT) or positron emission (PET) scanner, revealing spatial and temporal distribution of target-specific radiotracers and pharmaceuticals. An extensive array of radiopharmaceuticals, or molecular probes exist (based on ^{11}C, ^{13}N, ^{15}O, ^{18}F, ^{124}I, ^{64}Cu, ^{68}Ga, and ^{89}Zr for PET and ^{123}I, ^{99m}Tc, ^{201}Ti, and ^{111}In for SPECT), to image diverse aspects of tumor physiology and biology. Data can reveal properties such as glucose metabolism, blood volume and flow, tissue uptake, receptor binding, and oxygen utilization. Because both modalities have relatively low spatial resolution, CT is usually added for an anatomic overlay of the biodistribution of the radiolabeled probe. Metabolic PET: ^{18}FDG-PET is the most established metabolic cancer imaging approach both preclinically and clinically. Most tumors have a highly glycolytic phenotype (the Warburg effect), providing the basis for increased uptake and accumulation of the radioactive glucose analogue ^{18}FDG, as shown in various mouse models of leukemia, pancreatic, lung, colorectal, breast, prostate cancers (**Fig. 1D**, **15**; refs. 51, 129–132). Other tracers have recently been introduced to elucidate abnormal metabolic phenotypes, including, either ^{11}C- or ^{18}F-, acetate (mitochondrial metabolism; ref. 133), choline (membrane phospholipids; refs. 133, 134), and amino acids in brain tumors (glutamine, tyrosine, or methionine; **Fig. 1D**, **16**; refs. 135–138). Physiologic PET: several essential ^{18}F-labeled tracers should be mentioned here as potential (although not entirely specific) markers for tumor cell proliferation (^{18}F-fluorothymidine, ^{18}FLT) and hypoxia (18F-fluoroazomycin arabinoside, ^{18}F-FAZA, and ^{18}F-fluoromisonidazole, ^{18}F-MISO). Radioactive thymidine is readily incorporated into DNA synthesis, making an increased uptake of ^{18}FLT visible on animal PET and correlating with increased ADC on diffusion-weighted MRI, albeit exhibiting low specificity (139–142). ^{18}F-MISO is trapped in hypoxic areas as compared with BOLD and TOLD MRI (**Fig. 1B**, **10**; ref. 143). While ^{18}F-MISO has been tested for many years, its uptake selectivity is suboptimal and many other potential hypoxia-imaging agents are under development and evaluation (e.g., ^{18}F-FAZA shows more rapid background clearance; refs. 144, 145). Cellular PET: with the development of checkpoint inhibitor and immunotherapies, significant efforts have been dedicated to develop so-called "immunoPET." Several T lymphocyte–targeting molecules were radiochemically labeled with long-lived radionuclides (such as ^{64}Cu, ^{68}Ga, and ^{89}Zr). Following intravenous injection, intratumoral accumulation of T lymphocytes has been noninvasively detected in response to checkpoint inhibitor treatment (**Fig. 1E**, **20**; refs. 146–148). Molecular PET/SPECT: specific molecular targets have been visualized using PET- or SPECT-based peptides, antibodies, and receptor binding ligands. One of the most explored is hormone imaging, ^{18}F-fluoroestradiol PET, as used for preclinical and clinical imaging of estrogen receptor–positive (ER^+) breast and ovarian cancer (**Fig. 1F**, **24**; refs. 149–152). Recent examples of hormone imaging include PET of androgen receptor in rat brain (153). Several ^{111}In/^{203}Pb-labeled peptides for SPECT (154) and ^{68}Ga-MSH for PET (155) have been developed to target the melanocortin-1 receptor in melanoma mouse models (**Fig. 1F**, **25**). A ^{203}Pb/^{212}Pb theranostic pair has been reported for PSMA-based α-particle–targeted radiopharmaceutical therapy in advanced prostate cancer (156).

Other notable imaging technologies include magnetic particle imaging (MPI) and electron spin resonance (ESR). MPI is an emerging imaging modality that involves iron oxide nanoparticles. Unlike MRI, MPI measures electronic moment of particles, which is more sensitive than measuring changes in proton relaxation by MRI. The detection is linear, sensitive (ng of iron/voxel), and has a high signal-to-background ratio. Using MPI of iron oxide particles, kinetics of accumulation of nanoparticles in rat tumors (157) and kinetics of drug release in mouse breast tumors (158) were studied. Further applications of MPI are dependent on improving the acquisition speed and resolution, as well as improving circulation and targeting properties of nanoparticles.

Electron paramagnetic resonance (EPR), also termed as ESR, has been a research tool for many years, but remains somewhat esoteric in cancer research, largely due to lack of available instrumentation. It directly detects free radicals, but the extremely high frequencies tend to limit tissue penetration, although effective studies have been performed in mice and human teeth and tattoos (159). The most popular application has been based on imaging signal line width and relaxation mechanisms, which may be directly responsive to the presence of oxygen and hence, pO_2. Reporter agents may be injected directly into tumors (e.g., India ink or chars; ref. 160), or infused systemically (OX63- oxygen-measuring spin probe, coincidently the same material is used to achieve hyperpolarization of ^{13}C substrates for nuclear magnetic resonance; ref. 161). Sensitivity to oxygen can be particularly high at very low, radiobiologically relevant pO_2 values (0–15 Torr) and significant correlations have been observed between pO_2 values and radiation response (50, 160–162). A significant drawback of EPR is the lack of integrated anatomic information, generally requiring that separate MRI be performed and coregistered.

Published OnlineFirst December 1, 2020; DOI: 10.1158/0008-5472.CAN-20-0373

Image-Guided Irradiation

Radiation plays an important role in cancer therapy; radiation-based therapy has been applied to animal models for decades and recently has undergone significant improvement in terms of applying multimodality imaging to guide radiation planning (163, 164). Radiation kills cancer cells by damaging DNA, either directly or indirectly, through the creation of reactive oxygen species. Because radiation kills both cancer cells and healthy cells alike, various methods are used to increase the tumoricidal effects of radiation while minimizing damage to the surrounding normal tissue, including spatial modulation of the dose distribution to conform to a specific target region. While such conformal dose distributions allow for significant reductions in normal tissue toxicity, they also require onboard image guidance systems to ensure the tumor is in the correct location when the radiation beam is turned on. Modern animal irradiators incorporate multimodal imaging detectors to precisely guide the radiation, combining the ability to deliver targeted radiation treatments using a 225 kVp, gantry-mounted X-ray tube with digital radiography, fluoroscopy, cone-beam CT, and BLI (164, 165). Image-guided irradiation has been successfully applied even for small orthotopic head and neck and lung lesions in tumor-bearing mice (166, 167). The software also allows import of existing imaging datasets from other modalities, such as MRI, which often plays a crucial role for irradiating intracranial brain tumor models (9, 163).

Image Analysis and Quantitative Biomarkers

There is increasing interest in using imaging to develop noninvasive quantitative imaging biomarkers (surrogate endpoints) for cancer characterization. Indeed, most imaging read-outs are provided in both qualitative and quantitative form (**Table 2**; ref. 168). This is especially true for MRI, CT, and US, due to their high spatial resolution to provide precise tumor dimensions, as well as number of suspicious lesions/metastases (169, 170). The well-established mathematical modeling algorithms for tracer kinetics allow quantification of tumor vasculature based on gadolinium, nanoparticle, and microbubble uptake for MRI, CT, and US, respectively (32, 34). The biomarkers include the exchange rate constants (K^{trans}), which reflect the efflux rate of gadolinium contrast from blood plasma into the tissue/tumor extravascular extracellular space, the volume of contrast agent distribution V_e, or simply the area under enhancement curves after the administration of contrast (19, 171–174). Finally, physiologic MRI provides established quantitative endpoints in the form of ADCs from diffusion-weighted MRI: low ADC ($0.5–0.8 \times 10^{-3}$ mm^2/second) indicates densely cellular aggressive tumors, while treatment-induced necrosis results in increased ADC, up to 1.2×10^{-3} mm^2/seconds, and radiation-induced edema's ADC as high as 2.2 mm^2/second (17, 19). PET and SPECT tracer uptake is usually reported as standard uptake values (SUV), which includes normalization to injected dose and accounts for radionuclide decay (129, 130, 175). Several studies report ratios of signal intensities (SI) of the tumor-to-normal tissue (most often for brain tumors as tumor-to-brain ratios; refs. 138, 174). Optical imaging (BLI and FLI) is rather semiquantitative, but can provide SIs related to tumor volume or tissue perfusion (11, 114), for example, the change in light emission from luciferase-expressing tumors following an acute intervention, such as a vascular disrupting agent (VDA) provides an indication of vascular shutdown (101, 176, 177). Multimodality imaging ideally combines the advantages of each modality, while mitigating their deficiencies. Image registration is necessary when more than one imaging modality is used. Histology can often serve as the ground-truth for the validation of image-based biomarkers or new imaging modalities.

Identifying noninvasive biomarkers to be used clinically as surrogate endpoints is not only valuable, but also promising. The advent of machine learning and artificial intelligence in medical imaging has led to the field of radiomics (170, 178–181). Like genomics and other "-omics," radiomics allows quantifiable characterization of image features that provide a means to identify image-based biomarker surrogates for response to cancer treatment. Cameron and colleagues report a radiomics method, based on morphology, asymmetry, physiology, and size (MAPS) using multiparametric MRI (182). Most radiomics data have been reported for multicenter human studies, because a large number of subjects needs to be enrolled, the number of experimental animals in a single-imaging study often being a limiting factor. As quantitative imaging and radiomics lead to more image-based biomarkers, standardization and assessment of reproducibility are becoming important and will require a centralized image archive for multicenter preclinical studies.

Future Directions in Translational Imaging

Imaging is highly translational by nature and murine models have contributed enormously to the development of oncologic imaging methodologies (183). However, the complex, heterogeneous tumor microenvironment observed in human cancer is challenging to model in an immunodeficient animal system, particularly in terms of immunotherapeutic strategies. Lack of optimal preclinical models for testing is likely responsible for the dismal success rate (5%–8%) of cancer therapeutics developed in murine models to eventually obtain FDA approval for use in human patients (184). Dogs with naturally occurring cancers provide an alternative, complementary system for preclinical cancer research. The recent completion of the sequencing of the dog genome has shown that most of their 19,000 genes are orthologous or similar to humans (185). Companion animals live in our homes and are exposed to similar environmental and lifestyle influences. Their cancers grow slowly in an immunocompetent milieu, allowing for complex carcinogenesis, genomic instability, and immune avoidance to develop. Their size is such that serial biologic sampling can be performed before, during, and after therapy. These patients are imaged in human equipment, allowing for standardization of imaging protocols, improved spatial resolution for more accurate quantitative analysis, and adequate quality assurance of biodistribution for novel imaging probes. Power Doppler US and contrast-enhanced US were used to demonstrate tumor vascular response to antivascular therapy in canine patients with cancer noninvasively (186). There are several success stories to report today: ^{18}FDG- and ^{18}F-NaF PET/CT have been successfully used in canine patients with cancer to detect head and neck cancer and bone involvement of the nasal cavity (**Fig. 1F**, **23**; ref. 187). An iodinated nanoparticle CT tracer, initially developed and validated in a murine lung cancer model (described above; ref. 73), has been successfully used in a CT study of companion dogs with spontaneous tumors (188). An anatomic and functional imaging probe for a novel immunotherapeutic was developed in dogs with spontaneous lymphoma (189). A recombinant oncolytic vesicular stomatitis virus that expresses a surface sodium-iodide symporter (NIS) protein and IFNβ was characterized. On the basis of clinical response to VSV-IFNβ-NIS therapy in dogs with T-cell lymphoma, a phase I clinical trial in people has been started (NCT03017820; ref. 189). In a follow-up

Published OnlineFirst December 1, 2020; DOI: 10.1158/0008-5472.CAN-20-0373

study, dogs administered with VSV-IFNβ-NIS were evaluated to determine whether ^{18}F-tetrafluoroborate radiopharmaceutical that binds to the cell surface NIS can be used to confirm successful viral gene replication (190). Veterinary patients with naturally occurring cancers may assist in the development of new molecular imaging probes, shorten the approval process of oncologic therapies, and create a mutually beneficial bridge between the fields of veterinary and human oncology.

In summary, multimodal oncologic imaging has become a cutting-edge necessity in preclinical (animal) cancer research. Understanding the physical principles of each modality is essential for applying the correct noninvasive imaging protocol to an animal-based study. Development of imaging probes for multimodal imaging technologies is also an important scientific and clinical goal. Each imaging modality brings specific insights into oncological questions and allows researchers to follow the biology, dictating the choice of the optimal reporter and imaging modality to best characterize cancer phenotype (191). The future also holds a big promise for PET/MRI (similarly to existing PET/CT), combining two powerful molecular, physiologic, and structural techniques into one scanner. Finally, we anticipate the introduction of novel predictive models and deep-learning algorithms (192) in the near future for managing sophisticated and complex image datasets in animal models of cancer.

Authors' Disclosures

M. Farhoud reports personal fees from Emit Imaging (employment) outside the submitted work. A. De Lille reports personal fees from UC Denver (honorarium) during the conduct of the study, SonoVol, Inc (employment and share-holder), and PerkinElmer (employment and share-holder) outside the submitted work. D. Simberg reports grants from NIH during the conduct of the study. L. Griffin reports nonfinancial support from AMAG Pharmaceuticals [provided medication (Feraheme) for a grant from Morris Animal Foundation; not related to this study] outside the submitted work. R.P. Mason reports grants from NCI P30 CA142543, NIH S10 OD018094-01A1, CPRIT RP120670-P3, and NCI R01 CA140674 during the conduct of the study. N.J. Serkova reports grants from NCI P30 CA046934, NIH UL1 TR002535, NIH S10 023485, NIH S10 027023, and SBF 639631. No disclosures were reported by the other authors.

Acknowledgments

This review was based on the 2019 Animal Imaging Workshop held at the University of Colorado Anschutz Medical Campus. The workshop was partly supported by the NIH Shared Instrumentation Grant Program (S10 OD023485, S10 OD023491, S10 OD027023, and S10 OD018094), the University of Colorado and the University of Southwestern CCSG Cancer Center grants (P30 CA046934 and CA142543, respectively), the University of Colorado Clinical Translational Institute (UL1 TR002535), and the Nutritional and Obesity Research Center (P30 DK048520).

Received February 4, 2020; revised June 10, 2020; accepted November 25, 2020; published first December 1, 2020.

References

1. de Jong M, Essers J, van Weerden WM. Imaging preclinical tumour models: improving translational power. Nat Rev Cancer 2014;14:481–93.
2. Jardim-Perassi BV, Huang S, Dominguez-Viqueira W, Poleszczuk J, Budzevich MM, Abdalah MA, et al. Multiparametric MRI and coregistered histology identify tumor habitats in breast cancer mouse models. Cancer Res 2019;79:3952–64.
3. Weissleder R, Schwaiger MC, Gambhir SS, Hricak H. Imaging approaches to optimize molecular therapies. Sci Transl Med 2016;8:355ps16.
4. Condeelis J, Weissleder R. *In vivo* imaging in cancer. Cold Spring Harb Perspect Biol 2010;2:a003848.
5. Hausner SH, Bold RJ, Cheuy LY, Chew HK, Daly ME, Davis RA, et al. Preclinical development and first-in-human imaging of the integrin alphavbeta6 with [(18)F]alphavbeta6-binding peptide in metastatic carcinoma. Clin Cancer Res 2019;25:1206–15.
6. Hormuth DA II, Sorace AG, Virostko J, Abramson RG, Bhujwalla ZM, Enriquez-Navas P, et al. Translating preclinical MRI methods to clinical oncology. J Magn Reson Imaging 2019;50:1377–92.
7. Wessels JT, Busse AC, Mahrt J, Dullin C, Grabbe E, Mueller GA. *In vivo* imaging in experimental preclinical tumor research–a review. Cytometry A 2007;71:542–9.
8. Mannheim JG, Kara F, Doorduin J, Fuchs K, Reischl G, Liang S, et al. Standardization of small animal imaging-current status and future prospects. Mol Imaging Biol 2018;20:716–31.
9. Pierce AM, Witt DA, Donson AM, Gilani A, Sanford B, Sill M, et al. Establishment of patient-derived orthotopic xenograft model of 1q+ posterior fossa group A ependymoma. Neuro Oncol 2019;21:1540–51.
10. Veo B, Danis E, Pierce A, Sola I, Wang D, Foreman NK, et al. Combined functional genomic and chemical screens identify SETD8 as a therapeutic target in MYC-driven medulloblastoma. JCI Insight 2019;4:e122933.
11. Green AL, DeSisto J, Flannery P, Lemma R, Knox A, Lemieux M, et al. BPTF regulates growth of adult and pediatric high-grade glioma through the MYC pathway. Oncogene 2020;39:2305–27.
12. Sartorius CA, Hanna CT, Gril B, Cruz H, Serkova NJ, Huber KM, et al. Estrogen promotes the brain metastatic colonization of triple negative breast cancer cells via an astrocyte-mediated paracrine mechanism. Oncogene 2016;35:2881–92.
13. Boult JKR, Apps JR, Holsken A, Hutchinson JC, Carreno G, Danielson LS, et al. Preclinical transgenic and patient-derived xenograft models recapitulate the radiological features of human adamantinomatous craniopharyngioma. Brain Pathol 2018;28:475–83.
14. Boult JKR, Box G, Vinci M, Perryman L, Eccles SA, Jones C, et al. Evaluation of the response of intracranial xenografts to VEGF signaling inhibition using multiparametric MRI. Neoplasia 2017;19:684–94.
15. Deep G, Kumar R, Nambiar DK, Jain AK, Ramteke AM, Serkova NJ, et al. Silibinin inhibits hypoxia-induced HIF-1α-mediated signaling, angiogenesis and lipogenesis in prostate cancer cells: *in vitro* evidence and *in vivo* functional imaging and metabolomics. Mol Carcinog 2017;56:833–48.
16. Heid I, Steiger K, Trajkovic-Arsic M, Settles M, Esswein MR, Erkan M, et al. Co-clinical assessment of tumor cellularity in pancreatic cancer. Clin Cancer Res 2017;23:1461–70.
17. Wu L, Li J, Fu C, Kuhn B, Wang X. Chemotherapy response of pancreatic cancer by diffusion-weighted imaging (DWI) and intravoxel incoherent motion DWI (IVIM-DWI) in an orthotopic mouse model. MAGMA 2019;32:501–9.
18. Chung YH, Yu CF, Chiu SC, Chiu H, Hsu ST, Wu CR, et al. Diffusion-weighted MRI and (18)F-FDG PET correlation with immunity in early radiotherapy response in BNL hepatocellular carcinoma mouse model: timeline validation. Eur J Nucl Med Mol Imaging 2019;46:1733–44.
19. Crowe W, Wang L, Zhang Z, Varagic J, Bourland JD, Chan MD, et al. MRI evaluation of the effects of whole brain radiotherapy on breast cancer brain metastasis. Int J Radiat Biol 2019;95:338–46.
20. Gore JC, Li M, Gao Y, Wu TL, Schilling KG, Huang Y, et al. Functional MRI and resting state connectivity in white matter - a mini-review. Magn Reson Imaging 2019;63:1–11.
21. O'Connor JPB, Robinson SP, Waterton JC. Imaging tumour hypoxia with oxygen-enhanced MRI and BOLD MRI. Br J Radiol 2019;92:20180642.
22. Panek R, Welsh L, Baker LCJ, Schmidt MA, Wong KH, Riddell AM, et al. Noninvasive imaging of cycling hypoxia in head and neck cancer using intrinsic susceptibility MRI. Clin Cancer Res 2017;23:4233–41.
23. Zhou H, Belzile O, Zhang Z, Wagner J, Ahn C, Richardson JA, et al. The effect of flow on blood oxygen level dependent (R(*) 2) MRI of orthotopic lung tumors. Magn Reson Med 2019;81:3787–97.
24. White DA, Zhang Z, Li L, Gerberich J, Stojadinovic S, Peschke P, et al. Developing oxygen-enhanced magnetic resonance imaging as a prognostic biomarker of radiation response. Cancer Lett 2016;380:69–77.
25. Yang DM, Arai TJ, Campbell JW III, Gerberich JL, Zhou H, Mason RP. Oxygen-sensitive MRI assessment of tumor response to hypoxic gas breathing challenge. NMR Biomed 2019;32:e4101.
26. Beeman SC, Shui YB, Perez-Torres CJ, Engelbach JA, Ackerman JJ, Garbow JR. O_2 -sensitive MRI distinguishes brain tumor versus radiation necrosis in murine models. Magn Reson Med 2016;75:2442–7.

Published OnlineFirst December 1, 2020; DOI: 10.1158/0008-5472.CAN-20-0373

27. Colliez F, Gallez B, Jordan BF. Assessing tumor oxygenation for predicting outcome in radiation oncology: a review of studies correlating tumor hypoxic status and outcome in the preclinical and clinical settings. Front Oncol 2017;7:10.
28. Hallac RR, Zhou H, Pidikiti R, Song K, Stojadinovic S, Zhao D, et al. Correlations of noninvasive BOLD and TOLD MRI with pO2 and relevance to tumor radiation response. Magn Reson Med 2014;71:1863–73.
29. Zhou H, Hallac RR, Yuan Q, Ding Y, Zhang Z, Xie XJ, et al. Incorporating oxygen-enhanced MRI into multi-parametric assessment of human prostate cancer. Diagnostics 2017;7:48.
30. Doblas S, He T, Saunders D, Pearson J, Hoyle J, Smith N, et al. Glioma morphology and tumor-induced vascular alterations revealed in seven rodent glioma models by in vivo magnetic resonance imaging and angiography. J Magn Reson Imaging 2010;32:267–75.
31. Kannan P, Kretzschmar WW, Winter H, Warren D, Bates R, Allen PD, et al. Functional parameters derived from magnetic resonance imaging reflect vascular morphology in preclinical tumors and in human liver metastases. Clin Cancer Res 2018;24:4694–704.
32. Robinson SP, Boult JKR, Vasudev NS, Reynolds AR. Monitoring the vascular response and resistance to sunitinib in renal cell carcinoma *in vivo* with susceptibility contrast MRI. Cancer Res 2017;77:4127–34.
33. Raina K, Ravichandran K, Rajamanickam S, Huber KM, Serkova NJ, Agarwal R. Inositol hexaphosphate inhibits tumor growth, vascularity, and metabolism in TRAMP mice: a multiparametric magnetic resonance study. Cancer Prev Res 2013;6:40–50.
34. Zormpas-Petridis K, Jerome NP, Blackledge MD, Carceller F, Poon E, Clarke M, et al. MRI imaging of the hemodynamic vasculature of neuroblastoma predicts response to antiangiogenic treatment. Cancer Res 2019;79:2978–91.
35. Murrell DH, Zarghami N, Jensen MD, Dickson F, Chambers AF, Wong E, et al. MRI surveillance of cancer cell fate in a brain metastasis model after early radiotherapy. Magn Reson Med 2017;78:1506–12.
36. Daldrup-Link HE, Golovko D, Ruffell B, Denardo DG, Castaneda R, Ansari C, et al. MRI of tumor-associated macrophages with clinically applicable iron oxide nanoparticles. Clin Cancer Res 2011;17:5695–704.
37. Serkova NJ. Nanoparticle-based magnetic resonance imaging on tumor-associated macrophages and inflammation. Front Immunol 2017;8:590.
38. Makela AV, Gaudet JM, Foster PJ. Quantifying tumor associated macrophages in breast cancer: a comparison of iron and fluorine-based MRI cell tracking. Sci Rep 2017;7:42109.
39. Chen TJ, Cheng TH, Chen CY, Hsu SC, Cheng TL, Liu GC, et al. Targeted Herceptin-dextran iron oxide nanoparticles for noninvasive imaging of HER2/neu receptors using MRI. J Biol Inorg Chem 2009;14:253–60.
40. Zhang Y, Ni Q, Xu C, Wan B, Geng Y, Zheng G, et al. Smart bacterial magnetic nanoparticles for tumor-targeting magnetic resonance imaging of HER2-positive breast cancers. ACS Appl Mater Interfaces 2019;11:3654–65.
41. Serkova NJ, Renner B, Larsen BA, Stoldt CR, Hasebroock KM, Bradshaw-Pierce EL, et al. Renal inflammation: targeted iron oxide nanoparticles for molecular MR imaging in mice. Radiology 2010;255:517–26.
42. Tse BW, Cowin GJ, Soekmadji C, Jovanovic L, Vasireddy RS, Ling MT, et al. PSMA-targeting iron oxide magnetic nanoparticles enhance MRI of preclinical prostate cancer. Nanomedicine 2015;10:375–86.
43. Ngen EJ, Benham Azad B, Boinapally S, Lisok A, Brummet M, Jacob D, et al. MRI assessment of prostate-specific membrane antigen (PSMA) targeting by a PSMA-targeted magnetic nanoparticle: potential for image-guided therapy. Mol Pharm 2019;16:2060–8.
44. Liu G, Banerjee SR, Yang X, Yadav N, Lisok A, Jablonska A, et al. A dextran-based probe for the targeted magnetic resonance imaging of tumours expressing prostate-specific membrane antigen. Nat Biomed Eng 2017;1:977–82.
45. Andronesi OC, Arrillaga-Romany IC, Ly KI, Bogner W, Ratai EM, Reitz K, et al. Pharmacodynamics of mutant-IDH1 inhibitors in glioma patients probed by *in vivo* 3D MRS imaging of 2-hydroxyglutarate. Nat Commun 2018;9:1474.
46. Salamanca-Cardona L, Shah H, Poot AJ, Correa FM, Di Gialleonardo V, Lui H, et al. *In vivo* imaging of glutamine metabolism to the oncometabolite 2-hydroxyglutarate in IDH1/2 mutant tumors. Cell Metab 2017;26:830–41.
47. Mignion L, Acciardo S, Gourgue F, Joudiou N, Caignet X, Goebbels RM, et al. Metabolic imaging using hyperpolarized pyruvate-lactate exchange assesses response or resistance to the EGFR inhibitor cetuximab in patient-derived HNSCC xenografts. Clin Cancer Res 2020;26:1932–43.
48. Albers MJ, Bok R, Chen AP, Cunningham CH, Zierhut ML, Zhang VY, et al. Hyperpolarized 13C lactate, pyruvate, and alanine: noninvasive biomarkers for prostate cancer detection and grading. Cancer Res 2008;68:8607–15.
49. Cavallari E, Carrera C, Sorge M, Bonne G, Muchir A, Aime S, et al. The ^{13}C hyperpolarized pyruvate generated by ParaHydrogen detects the response of the heart to altered metabolism in real time. Sci Rep 2018;8:8366.
50. Matsumoto S, Kishimoto S, Saito K, Takakusagi Y, Munasinghe JP, Devasahayam N, et al. Metabolic and physiologic imaging biomarkers of the tumor microenvironment predict treatment outcome with radiation or a hypoxia-activated prodrug in mice. Cancer Res 2018;78:3783–92.
51. Hesketh RL, Wang J, Wright AJ, Lewis DY, Denton AE, Grenfell R, et al. Magnetic resonance imaging is more sensitive than PET for detecting treatment-induced cell death-dependent changes in glycolysis. Cancer Res 2019;79:3557–69.
52. Chan KW, Jiang L, Cheng M, Wijnen JP, Liu G, Huang P, et al. CEST-MRI detects metabolite levels altered by breast cancer cell aggressiveness and chemotherapy response. NMR Biomed 2016;29:806–16.
53. Han Z, Li Y, Zhang J, Liu J, Chen C, van Zijl PC, et al. Molecular imaging of deoxycytidine kinase activity using deoxycytidine-Enhanced CEST MRI. Cancer Res 2019;79:2775–83.
54. Zhou J, Tryggestad E, Wen Z, Lal B, Zhou T, Grossman R, et al. Differentiation between glioma and radiation necrosis using molecular magnetic resonance imaging of endogenous proteins and peptides. Nat Med 2011;17:130–4.
55. Sehgal AA, Li Y, Lal B, Yadav NN, Xu X, Xu J, et al. CEST MRI of 3-O-methyl-D-glucose uptake and accumulation in brain tumors. Magn Reson Med 2019;81:1993–2000.
56. Lindeman LR, Jones KM, High RA, Howison CM, Shubitz LF, Pagel MD. Differentiating lung cancer and infection based on measurements of extracellular pH with acidoCEST MRI. Sci Rep 2019;9:13002.
57. Longo DL, Dastru W, Digilio G, Keupp J, Langereis S, Lanzardo S, et al. Iopamidol as a responsive MRI-chemical exchange saturation transfer contrast agent for pH mapping of kidneys: *in vivo* studies in mice at 7 T. Magn Reson Med 2011;65:202–11.
58. Krikken E, van der Kemp WJM, Khlebnikov V, van Dalen T, Los M, van Laarhoven HWM, et al. Contradiction between amide-CEST signal and pH in breast cancer explained with metabolic MRI. NMR Biomed 2019;32:e4110.
59. Yu JX, Hallac RR, Chiguru S, Mason RP. New frontiers and developing applications in 19F NMR. Prog Nucl Magn Reson Spectrosc 2013;70:25–49.
60. Makela AV, Foster PJ. Imaging macrophage distribution and density in mammary tumors and lung metastases using fluorine-19 MRI cell tracking. Magn Reson Med 2018;80:1138–47.
61. Diepart C, Karroum O, Magat J, Feron O, Verrax J, Calderon PB, et al. Arsenic trioxide treatment decreases the oxygen consumption rate of tumor cells and radiosensitizes solid tumors. Cancer Res 2012;72:482–90.
62. Previdi S, Abbadessa G, Dalo F, France DS, Broggini M. Breast cancer-derived bone metastasis can be effectively reduced through specific c-MET inhibitor tivantinib (ARQ 197) and shRNA c-MET knockdown. Mol Cancer Ther 2012;11:214–23.
63. Previdi S, Scolari F, Chila R, Ricci F, Abbadessa G, Broggini M. Combination of the c-Met inhibitor tivantinib and zoledronic acid prevents tumor bone engraftment and inhibits progression of established bone metastases in a breast xenograft model. PLoS One 2013;8:e79101.
64. Ottewell PD, Wang N, Brown HK, Reeves KJ, Fowles CA, Croucher PI, et al. Zoledronic acid has differential antitumor activity in the pre- and postmenopausal bone microenvironment *in vivo*. Clin Cancer Res 2014;20:2922–32.
65. Holen I, Lefley DV, Francis SE, Rennicks S, Bradbury S, Coleman RE, et al. IL-1 drives breast cancer growth and bone metastasis *in vivo*. Oncotarget 2016;7:75571–84.
66. Wu EK, Eliseeva S, Rahimi H, Schwarz EM, Georas SN. Restrictive lung disease in TNF-transgenic mice: correlation of pulmonary function testing and micro-CT imaging. Exp Lung Res 2019;45:175–87.
67. Ruscitti F, Ravanetti F, Essers J, Ridwan Y, Belenkov S, Vos W, et al. Longitudinal assessment of bleomycin-induced lung fibrosis by micro-CT correlates with histological evaluation in mice. Multidiscip Respir Med 2017;12:8.
68. Sasaki M, Chubachi S, Kameyama N, Sato M, Haraguchi M, Miyazaki M, et al. Evaluation of cigarette smoke-induced emphysema in mice using quantitative micro-computed tomography. Am J Physiol Lung Cell Mol Physiol 2015;308:L1039–45.
69. Ramasamy K, Dwyer-Nield LD, Serkova NJ, Hasebroock KM, Tyagi A, Raina K, et al. Silibinin prevents lung tumorigenesis in wild-type but not in iNOS-/- mice: potential of real-time micro-CT in lung cancer chemoprevention studies. Clin Cancer Res 2011;17:753–61.

70. Deng L, Xiao SM, Qiang JW, Li YA, Zhang Y. Early lung adenocarcinoma in mice: micro-computed tomography manifestations and correlation with pathology. Transl Oncol 2017;10:311–7.
71. Hegab AE, Kameyama N, Kuroda A, Kagawa S, Yin Y, Ornitz D, et al. Using micro-computed tomography for the assessment of tumor development and follow-up of response to treatment in a mouse model of lung cancer. J Vis Exp 2016:53904. DOI: 10.3791/53904.
72. Badea CT, Athreya KK, Espinosa G, Clark D, Ghafoori AP, Li Y, et al. Computed tomography imaging of primary lung cancer in mice using a liposomal-iodinated contrast agent. PLoS One 2012;7:e34496.
73. Ashton JR, Clark DP, Moding EJ, Ghaghada K, Kirsch DG, West JL, et al. Dual-energy micro-CT functional imaging of primary lung cancer in mice using gold and iodine nanoparticle contrast agents: a validation study. PLoS One 2014;9:e88129.
74. Clark DP, Badea CT. Micro-CT of rodents: state-of-the-art and future perspectives. Phys Med 2014;30:619–34.
75. Ghaghada KB, Starosolski ZA, Lakoma A, Kaffes C, Agarwal S, Athreya KK, et al. Heterogeneous uptake of nanoparticles in mouse models of pediatric high-risk neuroblastoma. PLoS One 2016;11:e0165877.
76. Starosolski Z, Villamizar CA, Rendon D, Paldino MJ, Milewicz DM, Ghaghada KB, et al. Ultra high-resolution *in vivo* computed tomography imaging of mouse cerebrovasculature using a long circulating blood pool contrast agent. Sci Rep 2015;5:10178.
77. Badea CT, Clark DP, Holbrook M, Srivastava M, Mowery Y, Ghaghada KB. Functional imaging of tumor vasculature using iodine and gadolinium-based nanoparticle contrast agents: a comparison of spectral micro-CT using energy integrating and photon counting detectors. Phys Med Biol 2019;64:065007.
78. Czernuszewicz TJ, Papadopoulou V, Rojas JD, Rajamahendiran RM, Perdomo J, Butler J, et al. A new preclinical ultrasound platform for widefield 3D imaging of rodents. Rev Sci Instrum 2018;89:075107.
79. Zhou H, Zhao D. Ultrasound imaging-guided intracardiac injection to develop a mouse model of breast cancer brain metastases followed by longitudinal MRI. J Vis Exp 2014:51146. DOI: 10.3791/51146.
80. Sastra SA, Olive KP. Quantification of murine pancreatic tumors by high-resolution ultrasound. Methods Mol Biol 2013;980:249–66.
81. Goetze RG, Buchholz SM, Patil S, Petzold G, Ellenrieder V, Hessmann E, et al. Utilizing high resolution ultrasound to monitor tumor onset and growth in genetically engineered pancreatic cancer models. J Vis Exp 2018:56979. DOI: 10.3791/56979.
82. Rojas JD, Papadopoulou V, Czernuszewicz TJ, Rajamahendiran RM, Chytil A, Chiang YC, et al. Ultrasound measurement of vascular density to evaluate response to anti-angiogenic therapy in renal cell carcinoma. IEEE Trans Biomed Eng 2019;66:873–80.
83. Kasoji SK, Rivera JN, Gessner RC, Chang SX, Dayton PA. Early assessment of tumor response to radiation therapy using high-resolution quantitative micro-vascular ultrasound imaging. Theranostics 2018;8:156–68.
84. Zhou J, Wang H, Zhang H, Lutz AM, Tian L, Hristov D, et al. VEGFR2-targeted three-dimensional ultrasound imaging can predict responses to antiangiogenic therapy in preclinical models of colon cancer. Cancer Res 2016;76:4081–9.
85. Fix SM, Papadopoulou V, Velds H, Kasoji SK, Rivera JN, Borden MA, et al. Oxygen microbubbles improve radiotherapy tumor control in a rat fibrosarcoma model - a preliminary study. PLoS One 2018;13:e0195667.
86. Song KH, Trudeau T, Kar A, Borden MA, Gutierrez-Hartmann A. Ultrasound-mediated delivery of siESE complexed with microbubbles attenuates HER2+/- cell line proliferation and tumor growth in rodent models of breast cancer. Nanotheranostics 2019;3:212–22.
87. Xing L, Shi Q, Zheng K, Shen M, Ma J, Li F, et al. Ultrasound-mediated microbubble destruction (UMMD) facilitates the delivery of CA19-9 targeted and paclitaxel loaded mPEG-PLGA-PLL nanoparticles in pancreatic cancer. Theranostics 2016;6:1573–87.
88. Tran WT, Sannachi L, Papanicolau N, Tadayyon H, Al Mahrouki A, El Kaffas A, et al. Quantitative ultrasound imaging of therapy response in bladder cancer *in vivo*. Oncoscience 2016;3:122–33.
89. Rowles JL III, Han A, Miller RJ, Kelly JR, Applegate CC, Wallig MA, et al. Low fat but not soy protein isolate was an effective intervention to reduce nonalcoholic fatty liver disease progression in C57BL/6J mice: monitored by a novel quantitative ultrasound (QUS) method. Nutr Res 2019;63:95–105.
90. Elyas E, Papaevangelou E, Alles EJ, Erler JT, Cox TR, Robinson SP, et al. Correlation of ultrasound shear wave elastography with pathological analysis in a xenografic tumour model. Sci Rep 2017;7:165.
91. Riegler J, Labyed Y, Rosenzweig S, Javinal V, Castiglioni A, Dominguez CX, et al. Tumor elastography and its association with collagen and the tumor microenvironment. Clin Cancer Res 2018;24:4455–67.
92. Ahmed R, Ye J, Gerber SA, Linehan DC, Doyley MM. Preclinical imaging using single track location shear wave elastography: monitoring the progression of murine pancreatic tumor liver metastasis *in vivo*. IEEE Trans Med Imaging 2020;39:2426–39.
93. Taruttis A, van Dam GM, Ntziachristos V. Mesoscopic and macroscopic optoacoustic imaging of cancer. Cancer Res 2015;75:1548–59.
94. Zackrisson S, van de Ven S, Gambhir SS. Light in and sound out: emerging translational strategies for photoacoustic imaging. Cancer Res 2014;74:979–1004.
95. McNally LR, Mezera M, Morgan DE, Frederick PJ, Yang ES, Eltoum IE, et al. Current and emerging clinical applications of multispectral optoacoustic tomography (MSOT) in oncology. Clin Cancer Res 2016;22:3432–9.
96. Weber J, Beard PC, Bohndiek SE. Contrast agents for molecular photoacoustic imaging. Nat Methods 2016;13:639–50.
97. O'Kelly D, Zhou H, Mason RP. Tomographic breathing detection: a method to noninvasively assess in situ respiratory dynamics. J Biomed Opt 2018;23:1–6.
98. Cox B, Laufer JG, Arridge SR, Beard PC. Quantitative spectroscopic photoacoustic imaging: a review. J Biomed Opt 2012;17:061202.
99. O'Kelly D, Guo Y, Mason RP. Evaluating online filtering algorithms to enhance dynamic multispectral optoacoustic tomography. Photoacoustics 2020;19:100184.
100. Bohndiek SE, Sasportas LS, Machtaler S, Jokerst JV, Hori S, Gambhir SS. Photoacoustic tomography detects early vessel regression and normalization during ovarian tumor response to the antiangiogenic therapy trebananib. J Nucl Med 2015;56:1942–7.
101. Dey S, Kumari S, Kalainayakan SP, Campbell J III, Ghosh P, Zhou H, et al. The vascular disrupting agent combretastatin A-4 phosphate causes prolonged elevation of proteins involved in heme flux and function in resistant tumor cells. Oncotarget 2018;9:4090–101.
102. Tomaszewski MR, Gehrung M, Joseph J, Quiros-Gonzalez I, Disselhorst JA, Bohndiek SE. Oxygen-enhanced and dynamic contrast-enhanced optoacoustic tomography provide surrogate biomarkers of tumor vascular function, hypoxia, and necrosis. Cancer Res 2018;78:5980–91.
103. Rich LJ, Miller A, Singh AK, Seshadri M. Photoacoustic imaging as an early biomarker of radio therapeutic efficacy in head and neck cancer. Theranostics 2018;8:2064–78.
104. Hupple CW, Morscher S, Burton NC, Pagel MD, McNally LR, Cardenas-Rodriguez J. A light-fluence-independent method for the quantitative analysis of dynamic contrast-enhanced multispectral optoacoustic tomography (DCE MSOT). Photoacoustics 2018;10:54–64.
105. Zhou HL, Campbell J, O'Kelly D, Gerberich J, Mason R. Exploring a fluorescent blood pool agent in photoacoustic imaging. J Nucl Med 2016;57:1214.
106. Hudson SV, Huang JS, Yin W, Albeituni S, Rush J, Khanal A, et al. Targeted noninvasive imaging of EGFR-expressing orthotopic pancreatic cancer using multispectral optoacoustic tomography. Cancer Res 2014;74:6271–9.
107. Wu D, Huang L, Jiang MS, Jiang H. Contrast agents for photoacoustic and thermoacoustic imaging: a review. Int J Mol Sci 2014;15:23616–39.
108. Li L, Zemp RJ, Lungu G, Stoica G, Wang LV. Photoacoustic imaging of lacZ gene expression *in vivo*. J Biomed Opt 2007;12:020504.
109. Wang LV, Yao J. A practical guide to photoacoustic tomography in the life sciences. Nat Methods 2016;13:627–38.
110. Chan CM, Jing X, Pike LA, Zhou Q, Lim DJ, Sams SB, et al. Targeted inhibition of Src kinase with dasatinib blocks thyroid cancer growth and metastasis. Clin Cancer Res 2012;18:3580–91.
111. Boute N, Lowe P, Berger S, Malissard M, Robert A, Tesar M. NanoLuc luciferase - a multifunctional tool for high throughput antibody screening. Front Pharmacol 2016;7:27.
112. Duong MT, Collinson-Pautz MR, Morschl E, Lu A, Szymanski SP, Zhang M, et al. Two-dimensional regulation of CAR-T cell therapy with orthogonal switches. Mol Ther Oncolytics 2019;12:124–37.
113. Kleinovink JW, Mezzanotte L, Zambito G, Fransen MF, Cruz LJ, Verbeek JS, et al. A dual-color bioluminescence reporter mouse for simultaneous *in vivo* imaging of T cell localization and function. Front Immunol 2018;9:3097.

114. Contreras-Zarate MJ, Ormond DR, Gillen AE, Hanna C, Day NL, Serkova NJ, et al. Development of novel patient-derived xenografts from breast cancer brain metastases. Front Oncol 2017;7:252.
115. Godinat A, Bazhin AA, Goun EA. Bioorthogonal chemistry in bioluminescence imaging. Drug Discov Today 2018;23:1584–90.
116. Winn BA, Devkota L, Kuch B, MacDonough MT, Strecker TE, Wang Y, et al. Bioreductively activatable prodrug conjugates of combretastatin A-1 and combretastatin A-4 as anticancer agents targeted toward tumor-associated hypoxia. J Nat Prod 2020;83:937–54.
117. Chu J, Oh Y, Sens A, Ataie N, Dana H, Macklin JJ, et al. A bright cyan-excitable orange fluorescent protein facilitates dual-emission microscopy and enhances bioluminescence imaging *in vivo*. Nat Biotechnol 2016;34:760–7.
118. Hananya N, Shabat D. Recent advances and challenges in luminescent imaging: bright outlook for chemiluminescence of dioxetanes in water. ACS Cent Sci 2019;5:949–59.
119. Liu L, Mason RP. Imaging beta-galactosidase activity in human tumor xenografts and transgenic mice using a chemiluminescent substrate. PLoS One 2010; 5:e12024.
120. An W, Ryan LS, Reeves AG, Bruemmer KJ, Mouhaffel L, Gerberich JL, et al. A chemiluminescent probe for HNO quantification and real-time monitoring in living cells. Angew Chem Int Ed Engl 2019;58:1361–5.
121. Cao J, Lopez R, Thacker JM, Moon JY, Jiang C, Morris SN, et al. Chemiluminescent probes for imaging H2S in living animals. Chem Sci 2015;6:1979–85.
122. Lewis MA, Kodibagkar VD, Oz OK, Mason RP. On the potential for molecular imaging with Cerenkov luminescence. Opt Lett 2010;35:3889–91.
123. Pogue BW, Wilson BC. Optical and x-ray technology synergies enabling diagnostic and therapeutic applications in medicine. J Biomed Opt 2018;23: 1–17.
124. Zeng LJ, Zou LL, Yu HJ, He XY, Cao HQ, Zhang ZW, et al. Treatment of malignant brain tumor by tumor-triggered programmed wormlike micelles with precise targeting and deep penetration. Adv Funct Mater 2016;26: 4201–12.
125. Shaner NC, Campbell RE, Steinbach PA, Giepmans BNG, Palmer AE, Tsien RY. Improved monomeric red, orange and yellow fluorescent proteins derived from *Discosoma* sp. red fluorescent protein . Nat Biotechnol 2004;22:1567–72.
126. Zhong Y, Ma Z, Zhu S, Yue J, Zhang M, Antaris AL, et al. Boosting the downshifting luminescence of rare-earth nanocrystals for biological imaging beyond 1500 nm. Nat Commun 2017;8:737.
127. Ran C, Moore A. Spectral unmixing imaging of wavelength-responsive fluorescent probes: an application for the real-time report of amyloid beta species in Alzheimer's disease. Mol Imaging Biol 2012;14:293–300.
128. Hernot S, van Manen L, Debie P, Mieog JSD, Vahrmeijer AL. Latest developments in molecular tracers for fluorescence image-guided cancer surgery. Lancet Oncol 2019;20:e354–e67.
129. Ye H, Adane B, Khan N, Alexeev E, Nusbacher N, Minhajuddin M, et al. Subversion of systemic glucose metabolism as a mechanism to support the growth of leukemia cells. Cancer Cell 2018;34:659–73.
130. Shukla SK, Purohit V, Mehla K, Gunda V, Chaika NV, Vernucci E, et al. MUC1 and HIF-1alpha signaling crosstalk induces anabolic glucose metabolism to impart gemcitabine resistance to pancreatic cancer. Cancer Cell 2017;32:392.
131. Schlaepfer IR, Glode LM, Hitz CA, Pac CT, Boyle KE, Maroni P, et al. Inhibition of lipid oxidation increases glucose metabolism and enhances 2-Deoxy-2-[(18)F]Fluoro-D-Glucose uptake in prostate cancer mouse xenografts. Mol Imaging Biol 2015;17:529–38.
132. McKinley ET, Bugaj JE, Zhao P, Guleryuz S, Mantis C, Gokhale PC, et al. 18FDG-PET predicts pharmacodynamic response to OSI-906, a dual IGF-1R/IR inhibitor, in preclinical mouse models of lung cancer. Clin Cancer Res 2011; 17:3332–40.
133. Verwer EE, Kavanagh TR, Mischler WJ, Feng Y, Takahashi K, Wang S, et al. [(18)F]Fluorocholine and [(18)F]Fluoroacetate PET as imaging biomarkers to assess phosphatidylcholine and mitochondrial metabolism in preclinical models of TSC and LAM. Clin Cancer Res 2018;24:5925–38.
134. Witney TH, Alam IS, Turton DR, Smith G, Carroll L, Brickute D, et al. Evaluation of deuterated 18F- and 11C-labeled choline analogs for cancer detection by positron emission tomography. Clin Cancer Res 2012;18: 1063–72.
135. Wu Z, Zha Z, Li G, Lieberman BP, Choi SR, Ploessl K, et al. [(18)F](2S,4S)-4-(3-Fluoropropyl)glutamine as a tumor imaging agent. Mol Pharm 2014; 11:3852–66.
136. Ploessl K, Wang L, Lieberman BP, Qu W, Kung HF. Comparative evaluation of 18F-labeled glutamic acid and glutamine as tumor metabolic imaging agents. J Nucl Med 2012;53:1616–24.
137. Qu W, Oya S, Lieberman BP, Ploessl K, Wang L, Wise DR, et al. Preparation and characterization of L-[5-11C]-glutamine for metabolic imaging of tumors. J Nucl Med 2012;53:98–105.
138. Holzgreve A, Brendel M, Gu S, Carlsen J, Mille E, Boning G, et al. Monitoring of tumor growth with [(18)F]-FET PET in a mouse model of glioblastoma: SUV measurements and volumetric approaches. Front Neurosci 2016;10:260.
139. Morelli MP, Tentler JJ, Kulikowski GN, Tan AC, Bradshaw-Pierce EL, Pitts TM, et al. Preclinical activity of the rational combination of selumetinib (AZD6244) in combination with vorinostat in KRAS-mutant colorectal cancer models. Clin Cancer Res 2012;18:1051–62.
140. Honndorf VS, Schmidt H, Wiehr S, Wehrl HF, Quintanilla-Martinez L, Stahlschmidt A, et al. The synergistic effect of selumetinib/docetaxel combination therapy monitored by [(18) F]FDG/[(18) F]FLT PET and diffusion-weighted magnetic resonance imaging in a colorectal tumor xenograft model. Mol Imaging Biol 2016;18:249–57.
141. Zhang CC, Yan Z, Li W, Kuszpit K, Painter CL, Zhang Q, et al. [(18)F]FLT-PET imaging does not always "light up" proliferating tumor cells. Clin Cancer Res 2012;18:1303–12.
142. Chen W, Hill H, Christie A, Kim MS, Holloman E, Pavia-Jimenez A, et al. Targeting renal cell carcinoma with a HIF-2 antagonist. Nature 2016;539: 112–7.
143. Zhou H, Chiguru S, Hallac RR, Yang D, Hao G, Peschke P, et al. Examining correlations of oxygen sensitive MRI (BOLD/TOLD) with [(18)F]FMISO PET in rat prostate tumors. Am J Nucl Med Mol Imaging 2019;9:156–67.
144. Peeters SG, Zegers CM, Lieuwes NG, van Elmpt W, Eriksson J, van Dongen GA, et al. A comparative study of the hypoxia PET tracers [(1)(8)F]HX4, [(1)(8)F]FAZA, and [(1)(8)F]FMISO in a preclinical tumor model. Int J Radiat Oncol Biol Phys 2015;91:351–9.
145. Melsens E, De Vlieghere E, Descamps B, Vanhove C, Kersemans K, De Vos F, et al. Hypoxia imaging with (18)F-FAZA PET/CT predicts radiotherapy response in esophageal adenocarcinoma xenografts. Radiat Oncol 2018;13:39.
146. Levi J, Lam T, Goth SR, Yaghoubi S, Bates J, Ren G, et al. Imaging of activated t cells as an early predictor of immune response to anti-PD-1 therapy. Cancer Res 2019;79:3455–65.
147. Beckford Vera DR, Smith CC, Bixby LM, Glatt DM, Dunn SS, Saito R, et al. Immuno-PET imaging of tumor-infiltrating lymphocytes using zirconium-89 radiolabeled anti-CD3 antibody in immune-competent mice bearing syngeneic tumors. PLoS One 2018;13:e0193832.
148. Srideshikan SM, Brooks J, Zuro D, Kumar B, Sanchez J, Echavarria Parra L, et al. ImmunoPET, [(64)Cu]Cu-DOTA-Anti-CD33 PET-CT, imaging of an AML xenograft model. Clin Cancer Res 2019;25:7463–74.
149. Paquette M, Ouellet R, Archambault M, Croteau E, Lecomte R, Benard F. [18F]-fluoroestradiol quantitative PET imaging to differentiate ER+ and ERα-knockdown breast tumors in mice. Nucl Med Biol 2012;39:57–64.
150. Paquette M, Phoenix S, Ouellet R, Langlois R, van Lier JE, Turcotte EE, et al. Assessment of the novel estrogen receptor PET tracer 4-fluoro-11beta-methoxy-16alpha-[(18)F]fluoroestradiol (4FMFES) by PET imaging in a breast cancer murine model. Mol Imaging Biol 2013;15:625–32.
151. Fowler AM, Chan SR, Sharp TL, Fettig NM, Zhou D, Dence CS, et al. Small-animal PET of steroid hormone receptors predicts tumor response to endocrine therapy using a preclinical model of breast cancer. J Nucl Med 2012;53:1119–26.
152. Tsujikawa T, Yoshida Y, Kiyono Y, Kurokawa T, Kudo T, Fujibayashi Y, et al. Functional oestrogen receptor alpha imaging in endometrial carcinoma using 16alpha-[(1)(8)F]fluoro-17beta-oestradiol PET. Eur J Nucl Med Mol Imaging 2011;38:37–45.
153. Khayum MA, Doorduin J, Antunes IF, Kwizera C, Zijlma R, den Boer JA, et al. *In vivo* imaging of brain androgen receptors in rats: a [(18)F]FDHT PET study. Nucl Med Biol 2015;42:561–9.
154. Miao Y, Figueroa SD, Fisher DR, Moore HA, Testa RF, Hoffman TJ, et al. 203Pb-labeled alpha-melanocyte-stimulating hormone peptide as an imaging probe for melanoma detection. J Nucl Med 2008;49:823–9.
155. Yang J, Xu J, Gonzalez R, Lindner T, Kratochwil C, Miao Y. (68)Ga-DOTA-GGNle-CycMSHhex targets the melanocortin-1 receptor for melanoma imaging. Sci Transl Med 2018;10:eaau4445.
156. Banerjee SR, Minn I, Kumar V, Josefsson A, Lisok A, Brummet M, et al. Preclinical evaluation of 203/212Pb-labeled low-molecular-weight compounds for targeted radiopharmaceutical therapy of prostate cancer. J Nucl Med 2020; 61:80–8.

157. Yu EY, Bishop M, Zheng B, Ferguson RM, Khandhar AP, Kemp SJ, et al. Magnetic particle imaging: a novel *in vivo* imaging platform for cancer detection. Nano Lett 2017;17:1648–54.
158. Zhu X, Li J, Peng P, Hosseini Nassab N, Smith BR. Quantitative drug release monitoring in tumors of living subjects by magnetic particle imaging nanocomposite. Nano Lett 2019;19:6725–33.
159. Flood AB WV, Schreiber W, Williams BB, Gallez B, Swartz HM. Guidance to transfer 'Bench-Ready' medical technology into usual clinical practice: case study - sensors and spectrometer used in EPR oximetry. In: Thews O LJ, Harrison DK, editors. Oxygen transport to tissue Xl advances in experimental medicine and biology. Cham, Switzerland: Springer International Publishing Ag; 2018. p.233–9.
160. Goda F, O'Hara JA, Rhodes ES, Liu KJ, Dunn JF, Bacic G, et al. Changes of oxygen tension in experimental tumors after a single dose of X-ray irradiation. Cancer Res 1995;55:2249–52.
161. Epel B, Maggio MC, Barth ED, Miller RC, Pelizzari CA, Krzykawska-Serda M, et al. Oxygen-guided radiation therapy. Int J Radiat Oncol Biol Phys 2019;103:977–84.
162. Jordan BF, Gregoire V, Demeure RJ, Sonveaux P, Feron O, O'Hara J, et al. Insulin increases the sensitivity of tumors to irradiation: involvement of an increase in tumor oxygenation mediated by a nitric oxide-dependent decrease of the tumor cells oxygen consumption. Cancer Res 2002;62:3555–61.
163. Chiu TD, Arai TJ, Campbell Iii J, Jiang SB, Mason RP, Stojadinovic S. MR-CBCT image-guided system for radiotherapy of orthotopic rat prostate tumors. PLoS One 2018;13:e0198065.
164. Ghita M, Brown KH, Kelada OJ, Graves EE, Butterworth KT. Integrating small animal irradiators with functional imaging for advanced preclinical radiotherapy research. Cancers 2019;11:170.
165. Parodi K, Assmann W, Belka C, Bortfeldt J, Clevert DA, Dedes G, et al. Towards a novel small animal proton irradiation platform: the SIRMIO project. Acta Oncol 2019;58:1470–5.
166. Oweida AJ, Bhatia S, Van Court B, Darragh L, Serkova N, Karam SD. Intramucosal inoculation of squamous cell carcinoma cells in mice for tumor immune profiling and treatment response assessment. J Vis Exp 2019. DOI: 10.3791/59195.
167. Bhatia S, Oweida A, Lennon S, Darragh LB, Milner D, Phan AV, et al. Inhibition of EphB4-Ephrin-B2 signaling reprograms the tumor immune microenvironment in head and neck cancers. Cancer Res 2019;79:2722–35.
168. Keenan KE, Biller JR, Delfino JG, Boss MA, Does MD, Evelhoch JL, et al. Recommendations towards standards for quantitative MRI (qMRI) and outstanding needs. J Magn Reson Imaging 2019;49:e26–e39.
169. Turco S, Tardy I, Frinking P, Wijkstra H, Mischi M. Quantitative ultrasound molecular imaging by modeling the binding kinetics of targeted contrast agent. Phys Med Biol 2017;62:2449–64.
170. Hormuth DA II, Jarrett AM, Lima E, McKenna MT, Fuentes DT, Yankeelov TE. Mechanism-based modeling of tumor growth and treatment response constrained by multiparametric imaging data. JCO Clin Cancer Inform 2019;3:1–10.
171. Pitman KE, Bakke KM, Kristian A, Malinen E. Ultra-early changes in vascular parameters from dynamic contrast enhanced MRI of breast cancer xenografts following systemic therapy with doxorubicin and liver X receptor agonist. Cancer Imaging 2019;19:88.
172. Cao J, Pickup S, Clendenin C, Blouw B, Choi H, Kang D, et al. Dynamic contrast-enhanced MRI detects responses to stroma-directed therapy in mouse models of pancreatic ductal adenocarcinoma. Clin Cancer Res 2019;25:2314–22.
173. Fiegle E, Doleschel D, Koletnik S, Rix A, Weiskirchen R, Borkham-Kamphorst E, et al. Dual CTLA-4 and PD-L1 blockade inhibits tumor growth and liver metastasis in a highly aggressive orthotopic mouse model of colon cancer. Neoplasia 2019;21:932–44.
174. Scott AJ, Arcaroli JJ, Bagby SM, Yahn R, Huber KM, Serkova NJ, et al. Cabozantinib exhibits potent antitumor activity in colorectal cancer patient-derived tumor xenograft models via autophagy and signaling mechanisms. Mol Cancer Ther 2018;17:2112–22.
175. Dhar D, Raina K, Kant R, Wempe MF, Serkova NJ, Agarwal C, et al. Bitter melon juice-intake modulates glucose metabolism and lactate efflux in tumors in its efficacy against pancreatic cancer. Carcinogenesis 2019;40:1164–76.
176. Niu H, Strecker TE, Gerberich JL, Campbell JW III, Saha D, Mondal D, et al. Structure guided design, synthesis, and biological evaluation of novel benzosuberene analogues as inhibitors of tubulin polymerization. J Med Chem 2019;62:5594–615.
177. Bothwell KD, Folaron M, Seshadri M. Preclinical activity of the vascular disrupting agent OXi4503 against head and neck cancer. Cancers 2016;8:1–12.
178. Theek B, Opacic T, Magnuska Z, Lammers T, Kiessling F. Radiomic analysis of contrast-enhanced ultrasound data. Sci Rep 2018;8:11359.
179. Moiseev A, Snopova L, Kuznetsov S, Buyanova N, Elagin V, Sirotkina M, et al. Pixel classification method in optical coherence tomography for tumor segmentation and its complementary usage with OCT microangiography. J Biophotonics 2018;11:e201700072.
180. Zinn PO, Singh SK, Kotrotsou A, Hassan I, Thomas G, Luedi MM, et al. A coclinical radiogenomic validation study: conserved magnetic resonance radiomic appearance of periostin-expressing glioblastoma in patients and xenograft models. Clin Cancer Res 2018;24:6288–99.
181. Ellingson BM. On the promise of artificial intelligence for standardizing radiographic response assessment in gliomas. Neuro-oncol 2019;21:1346–7.
182. Cameron A, Khalvati F, Haider MA, Wong A. MAPS: a quantitative radiomics approach for prostate cancer detection. IEEE Trans Biomed Eng 2016;63:1145–56.
183. Dragani TA, Castells A, Kulasingam V, Diamandis EP, Earl H, Iams WT, et al. Major milestones in translational oncology. BMC Med 2016;14:110.
184. Mak IW, Evaniew N, Ghert M. Lost in translation: animal models and clinical trials in cancer treatment. Am J Transl Res 2014;6:114–8.
185. Tarone L, Barutello G, Iussich S, Giacobino D, Quaglino E, Buracco P, et al. Naturally occurring cancers in pet dogs as pre-clinical models for cancer immunotherapy. Cancer Immunol Immunother 2019;68:1839–53.
186. Abma E, Stock E, De Spiegelaere W, Van Brantegem L, Vanderperren K, Ni Y, et al. Power Doppler ultrasound and contrast-enhanced ultrasound demonstrate non-invasive tumour vascular response to anti-vascular therapy in canine cancer patients. Sci Rep 2019;9:9262.
187. Spriet M, Willcox JL, Culp WTN. Role of positron emission tomography in imaging of non-neurologic disorders of the head, neck, and teeth in veterinary medicine. Front Vet Sci 2019;6:180.
188. Ghaghada KB, Sato AF, Starosolski ZA, Berg J, Vail DM. Computed tomography imaging of solid tumors using a liposomal-iodine contrast agent in companion dogs with naturally occurring cancer. PLoS One 2016;11:e0152718.
189. Naik S, Galyon GD, Jenks NJ, Steele MB, Miller AC, Allstadt SD, et al. Comparative oncology evaluation of intravenous recombinant oncolytic vesicular stomatitis virus therapy in spontaneous canine cancer. Mol Cancer Ther 2018;17:316–26.
190. LeBlanc AK. Cancer and comparative imaging. ILAR J 2014;55:164–8.
191. Mezzanotte L, Aswendt M, Tennstaedt A, Hoeben R, Hoehn M, Lowik C. Evaluating reporter genes of different luciferases for optimized *in vivo* bioluminescence imaging of transplanted neural stem cells in the brain. Contrast Media Mol Imaging 2013;8:505–13.
192. Banzato T, Bernardini M, Cherubini GB, Zotti A. A methodological approach for deep learning to distinguish between meningiomas and gliomas on canine MR-images. BMC Vet Res 2018;14:317.

Published OnlineFirst December 1, 2020; DOI: 10.1158/0008-5472.CAN-20-0373

Cancer Research
The Journal of Cancer Research (1916–1930) | The American Journal of Cancer (1931–1940)

AACR American Association for Cancer Research

Preclinical Applications of Multi-Platform Imaging in Animal Models of Cancer

Natalie J. Serkova, Kristine Glunde, Chad R. Haney, et al.

Cancer Res 2021;81:1189-1200. Published OnlineFirst December 1, 2020.